



Comparative assessment of biochars from multiple sources based on persulfate activation capability: Role of iron component in enhancing thermal treatment effect on carbocatalytic performance

Sae In Suh^{a,1}, Heesoo Woo^{b,1}, So-Yeon Song^a, Dongjoo Park^a, Yong-Yoon Ahn^c, Eunju Kim^d, Hongshin Lee^a, Dong-Wan Kim^a, Changha Lee^e, Yong Sik Ok^f, Jaesang Lee^{a,*}

^a Civil, Environmental, and Architectural Engineering, Korea University, Seoul 02841, the Republic of Korea

^b Geo-technical Team, ECO Solution Business Unit, SK Ecoplant, Seoul 03143, the Republic of Korea

^c Korea Polar Research Institute (KOPRI), Incheon 21990, the Republic of Korea

^d Water Cycle Research Center, Korea Institute of Science and Technology, Seoul 02792, the Republic of Korea

^e Chemical and Biological Engineering, Seoul National University, Seoul 08826, Republic of Korea

^f Korea Biochar Research Center, APRU Sustainable Waste Management Program & Division of Environmental Science and Ecological Engineering, Korea University, Seoul 02841, the Republic of Korea

ARTICLE INFO

Keywords:

Biochar
Persulfate activation
Thermal annealing
Carbon-encapsulated iron
Non-radical oxidation

ABSTRACT

In this study, we explored the correlation between the catalytic activity of UK Biochar Research Center biochars (BCs) and their physicochemical properties, suggesting a potential role of endogenous iron in promoting their persulfate activation capability by heat treatment. A steady improvement in the persulfate activation efficiency with increasing annealing temperature was observed exclusively for iron-containing BCs (e.g., sewage sludge (SS) BCs). Along with increasing the Brunauer–Emmett–Teller surface area, thermal annealing formed carbon-wrapped iron particles on the SS BC surfaces, produced crystalline elemental iron and iron carbides, and caused an sp^3 -to- sp^2 conversion in the carbon phase. Comparing the annealed SS BCs in terms of the open circuit potential shift, electrical conductivity, and thermodynamic binding parameters showed that the heat-initiated modification enhanced the electron transfer-mediating capacity and surface affinity toward persulfate, which led to the beneficial effect of annealing on the carbocatalytic activity of iron-containing BCs for non-radical persulfate activation.

1. Introduction

Water professionals have been increasingly focusing on heterogeneous carbocatalysis as an appealing technique for the activation of peroxymonosulfate (PMS) and peroxydisulfate (PDS) (collectively referred to as persulfate). This is owing to (i) high performance in oxidative treatment, (ii) minimal secondary contamination from toxic component release, (iii) chemical durability and biocompatibility, and (iv) facile modification (e.g., heteroatom doping and functionalization) to tune physicochemical and structural properties [1–3]. Engineered carbonaceous nanomaterials, such as carbon nanotubes, graphene, and their derivatives, have been demonstrated to effectively treat organic contaminants by persulfate activation based on three reaction routes: oxidation induced by highly reactive radicals, such as hydroxyl ($\cdot\text{OH}$)

and sulfate radicals ($\text{SO}_4^{\cdot-}$) [4,5], singlet oxygenation [6], and mediated electron transfer [7,8]. Performance tests have shown that carbocatalysts are competitive to transition and noble metal-based activators [5, 9]. Their technical merits including insensitivity of the activation capacity to the type of persulfate precursor and high persulfate utilization efficiency have been suggested based on comparison with benchmark metal activators [1,3]. However, the high cost of manufactured carbon nanomaterials is a major hurdle in their field-application as viable persulfate activators. Accordingly, to promote the practicability of carbocatalytic persulfate activation, utilizing naturally occurring and waste-derived carbon-rich substances as the precursors has been frequently considered as a feasible approach [10,11].

Biochar (BC) is a high-carbon content byproduct (typically consisting of approximately 50–90 % carbon [12]) of the pyrolysis of biomass

* Corresponding author.

E-mail address: lee39@korea.ac.kr (J. Lee).

¹ These authors contributed equally to this work.

under oxygen-deficient conditions. This cost-effective carbocatalyst presents the potential for catalytic persulfate activation owing to its intrinsic characteristics. These include (i) electrical conductivity, (ii) abundance of oxygen-containing surface functional groups, (iii) large surface area (ranging from 8 to 800 m²/g [13,14]), and (iv) high affinity toward organics [10,11,15]. Particularly, the moderate electrical conductivity of BCs originating from the redox activity of its graphitic carbon, quinone moieties, and persistent free radicals (PFRs) [16], enables radical and non-radical degradative pathways via single and double electron transfer reactions involving persulfate, respectively [10,11,15]. Functional groups on the BC surfaces activate persulfate by multiple mechanisms [17–20]. Electron-rich carbonyl groups kinetically enhance non-radical oxidation by accelerating the self-decay of PMS (accompanied with singlet oxygen (¹O₂) production) [18,20] and inducing the formation of surface persulfate complexes as electron-transfer mediators [19]. The positive correlation between the surface density of hydroxyl and carboxyl groups and the efficacy of radical oxidation suggests their roles as redox-active sites in BC-mediated conversion of persulfate to SO₄^{•−} [17,21].

Thermal annealing of carbonaceous materials is often adopted to modulate *sp*²/*sp*³ carbon ratio [8], surface area [13], hydrophilicity [22], and type and surface density of functional groups [23]. Considering the aforementioned properties of BCs that exert a critical influence on the kinetics and mechanisms of persulfate activation, annealing is potential intelligent approach for upgrading a BC as a carbocatalyst for persulfate activation. This has been reflected in the recent demonstration of heat treatment increasing the efficacy of a BC for the catalytic oxidation of organics in the presence of persulfate by raising the degree of graphitization (i.e., *sp*³-to-*sp*² carbon phase conversion) (accompanied with electrical conductivity improvement) [24]. Other examples supporting this are increase in the surface densities of oxygen functional groups [21] and change in the nature of nitrogen-containing moieties (originating from nitrogen impurity during pyrolysis) caused by thermal treatment [25]. Specifically, graphitic N initiated persulfate activation not reliant on •OH/SO₄^{•−} generation by inducing a positive charge on the adjacent carbon atoms [26] whereas pyrrolic N and pyridinic N possessing lone-pair electrons offered Lewis base sites, thus causing the conversion of persulfate into SO₄^{•−} [27] or promoting the local sorption capacity [28]. However, all studies on the beneficial effect of post-heat treatment are based on the performance enhancement of a single type of BC with a specific chemical composition, and little is still known about how thermal annealing can tune the carbocatalytic activity of BCs and modify the primary degradative pathway(s) induced by BC-activated persulfate. Furthermore, the impact of mineral constituents, such as iron and calcium, warrants in-depth investigation, considering that metal oxides formed by the exposure of metal impurities to heat serve as secondary reactive sites for persulfate activation [29,30] and that selected metal components catalyze the carbon phase transformation [31]. In particular, metal impregnation, applied to promote the efficiency of BCs for redox reaction-based water treatment [32,33], involves the secondary pyrolysis subsequent to exposure of BCs to metal solutions, and the resultant iron/carbon composites decomposed organics through persulfate activation by yielding diverse reactive intermediates, such as SO₄^{•−}, ¹O₂, and high-valent metals [33–35]. This implies the possible switching of the major oxidant(s) after heat treatment of metal-containing BCs.

To address the knowledge gap existing in the variation of the effect of thermal annealing with the type of BC, in this study, we examined 12 standard BCs of five different origins (provided by UK Biochar Research Center (UKBRC)) and their annealed counterparts for oxidative organic degradation by persulfate activation. The properties required for a BC to be the best performing activator were explored and the roles of inorganic impurities in improving the catalytic activity of a BC via annealing were investigated. For these purposes, pristine and heat-treated BCs were characterized in terms of their morphological features, carbon and metal phases, and surface functionality. Moreover, their persulfate

activation efficiencies were correlated to their electron transfer-mediating capacity and binding affinity toward persulfate, determined by the magnitude of the negative shift of the open circuit potential (OCP) and isothermal titration calorimetry, respectively. Major degradative pathways were elucidated based on (i) the retarding effects of radical scavengers, (ii) multi-activity assessment using diverse model substrates, (iii) electron paramagnetic resonance (EPR) spectral features, and (iv) product distribution. Finally, the catalytic performance of the annealed BC was assessed based on the variation in the treatment efficiency during multiple use in PDS activation followed by thermal regeneration.

2. Materials and methods

2.1. Chemical reagents

The following reagent-grade chemicals were used in this study: potassium monopersulfate (Oxone®), sodium peroxydisulfate, acetaminophen (ACT), benzoic acid (BA), bisphenol A (BPA), carbamazepine (CBZ), 4-chlorophenol (4-CP), furfuryl alcohol (FFA), 4-hydroxybenzoic acid (4-HBA), nitrobenzene (NB), phenol (PH), 2,4,6-trichlorophenol (TCP), 2,2,6,6-tetramethyl-4-piperidone (TEMP), 5-*tert*-butoxycarbonyl-5-methyl-1-pyrroline *N*-oxide (BMPO), methanol (MeOH), *tert*-butanol (*t*-BuOH), sodium bromide, sodium bromate, sodium chloride, sodium phosphate monobasic, sodium phosphate dibasic, sodium sulfate, formaldehyde (HCHO), perchloric acid, sodium hydroxide, phosphoric acid, and acetonitrile. All chemicals except BMPO (ENZO Life Sciences, Inc.), MeOH (J.T. Baker), and acetonitrile (J.T. Baker) were purchased from Sigma-Aldrich and used without further purification. Ultrapure deionized water (>18 MΩ cm), produced by a Milli-Q Water Purification System (Millipore), was used to prepare all experimental solutions and suspensions.

2.2. Biochar-based activator preparation and characterization

A total of 12 standard BC samples of diverse origins were provided by the UKBRC at the School of Geosciences, University of Edinburgh, UK. These BCs used as persulfate activators or their precursors originated from the following biomass sources (the three-digit number denotes the pyrolysis temperature in nitrogen atmosphere): miscanthus straw pellets (MSP550, MSP700), mixed softwood pellets (SWP550, SWP700), oil seed rape straws (OSR550, OSR700), rice husk (RH550, RH700), sewage sludge pellets (SS550, SS700), and wheat straw pellets (WSP550, WSP700). To investigate the enhancing effect of heat treatment, pristine BCs were annealed for 2 h at varying temperatures (i.e., 700 °C, 900 °C, and 1100 °C) under a nitrogen flow rate of 0.2 L min^{−1}. BC annealing was also performed at 1200 °C and 1600 °C but in a vacuum furnace utilizing a graphite heating element. Specifically, samples placed in graphite crucibles were annealed in a stainless-steel heating chamber that was evacuated to a pressure of 10^{−3} Torr using a rotary vacuum pump. Acid treatment is typically applied to increase the surface area, create functional groups, or remove metal impurities. It was achieved by exposing the BCs to concentrated acids (~1 N)—HCl, H₂SO₄, HNO₃, and aqua regia (i.e., the binary mixture of HCl and HNO₃)—for 1 h, washing them with distilled water, and drying the resultant products at 60 °C for 24 h.

The morphological features of the pristine and modified BCs were analyzed by scanning electron microscopy (FE-SEM; FEI, Quanta FEG 250) and high-resolution transmission electron microscopy (HR-TEM; FEI, Titan 300 kV). Temperature-sensitive changes of the structural characteristics, defect density, and type and concentration of surface functionalities were monitored. For this purpose, X-ray diffraction (XRD; Rigaku D/Max-2500 V) using Cu-Kα radiation, Raman spectroscopy (LabRam ARAMIS, Horiba Jobin-Yvon) using an argon ion laser (excitation at 532 nm), and X-ray photoelectron spectroscopy (XPS; Ulvac-PHI, PHI 5000 VersaProbe) using a monochromatic Al-Kα X-ray source

(1486.6 eV) were employed, respectively. The Brunauer-Emmett-Teller (BET) surface areas of the pristine and modified BCs were estimated from N₂ adsorption isotherms obtained using a gas sorption analyzer (Quantachrome Instruments, Autosorb-Iq 25 T/MP) at −195.8 °C. The zeta potentials of the samples were monitored using a zeta potential and particle size analyzer (Otsuka Electronics, ELSZ-1000) under varying pH conditions.

The electron transfer-mediating capabilities of the BC samples were comparatively assessed based on the OCP shift at BC-based working electrodes on the sequential addition of 4-CP and PDS and the electrical conductivity of the BC samples. The OCP was measured in a divided cell containing aqueous phosphate buffer solution (0.1 M) using a potentiostat (PGSTAT302N, Autolab). The three-electrode configuration consisted of a BC-coated fluorine-doped tin oxide (FTO; Fine Chemical Industry Co.) electrode, Ag/AgCl electrode, and coiled platinum wire as the respective working, reference, and counter electrodes. The BC-based working electrode was produced according to the methods used to fabricate carbon material-coated FTO. Briefly, the catalyst ink was prepared by manually mixing 5 mg BC sample, 29 µL Nafion perfluorinated resin solution, and 400 µL isopropanol followed by ultrasonic homogenization. By drop casting, 5 µL catalyst ink was coated onto a 1.0 × 1.0 cm FTO substrate (cleansed by sequential sonication with acetone, ethanol, and distilled water for 30 min each and air-dried for 30 min prior to catalyst loading). BC deposition was repeated twice to ensure that the carbon activator in a sufficient concentration was surface-loaded on the FTO. Temporal changes in the OCP values were monitored upon successive addition of 4-CP and PDS as electron donor and acceptor, respectively. Electrical conductivity was measured by a custom-built homemade cell. A BC powder was taken in a die cylinder made of an electrically insulating glass and was stoppered by lower (cathode) and upper (anode) copper electrodes. From the slopes of the current-voltage characteristic curves (obtained as the potential was swept from −5 V to +5 V) in the range of −1 V to +1 V, electrical resistivity as the reciprocal of conductivity was determined as follows:

$$\rho = \frac{RA}{l}$$

where ρ , R , A , and l represent the resistivity, resistance, cross-sectional area of the cell, and thickness of the BC powder vertically held in the sample holder, respectively.

2.3. Experimental procedures and analytical methods

Oxidative and adsorptive removal of organic compounds were performed in a magnetically stirred cylindrical glass reactor with a volume of 50 mL at room temperature under air-equilibrated conditions. In general, the experimental suspensions comprised of 0.1 mM target substrate, 1 mM PDS, and a pristine or annealed BC at an initial loadings of 0.6 g/L or 0.2 g/L, respectively. For reasonable comparison of the pristine and thermally treated BCs, identical concentrations of 0.2 g/L were prepared. However, the catalytic activities of the annealed BCs were assessed at a threefold lower level than those of the pristine ones, to minimize the organic removal by sorption. To ensure that the pH level initially set as 7.0 marginally changed throughout the persulfate activation, 1 mM phosphate buffer was used. Sample aliquots (1 mL) were drawn from the reactor at predetermined time intervals using a 1-mL syringe, filtered using a 0.45 µm PTFE membrane (Millipore), and transferred to a 2-mL vial containing 1 µL MeOH (corresponding to ~25 mM in the sample solutions) as the radical quencher. Organic compounds were quantified by high-performance liquid chromatography (HPLC; Agilent Infinity 1260) equipped with a C-18 column (ZORBAX Eclipse XDB-C18) and a UV/Vis detector (G1314 F 1260VWD). The HCHO concentration (monitored to support the occurrence of MeOH oxidation) was determined by HPLC analysis subsequent to derivatization using acidified 2,4-dinitrophenylhydrazine solution. BrO₃[−]

evolution, used as an indirect indication of radical formation, was monitored by ion chromatography using a Dionex DX120 system equipped with a Dionex IonPac AS-14 and a conductivity detector. Temporal changes in the PDS concentration were monitored by spectrophotometrically quantifying iodine (formed by persulfate oxidation of iodide) at 352 nm [36]. Intermediates generated from 4-CP oxidation using BC-activated PDS were qualitatively analyzed by gas chromatography mass spectrometry (GC-MS; Agilent 6890/5973 GC/MSD system) equipped with a DB-5MS column (30 m × 0.25 mm, 0.25 µm; Agilent). The intermediate analysis was also conducted by a Q Exactive Hybrid Quadrupole-Orbitrap mass spectrometer (Thermo Fisher Scientific Inc.) in the negative electrospray ionization mode. The separation was performed in a Hypersil GOLD™ aQ column with a mobile phase comprising aqueous 0.1 % (v/v) formic acid solution and acetonitrile in a volume ratio of 60:40. The extent of organic mineralization was determined by monitoring the total organic carbon (TOC) reduction and the CO₂ evolution using a TOC analyzer (TOC-L, Shimadzu) and GC (GC-2010 Plus, Shimadzu) equipped with a 1.8 m × 3.2 mm stainless-steel column packed with a Porapak Q column (Restek Corporation) and a thermal conductivity detector (TCD), respectively. To identify the transient radical and non-radical species (i.e., PFRs, SO₄^{•−}, and ¹O₂), EPR spectra were acquired during BC-induced PDS activation using a JEOL JES-TE 300 spectrometer under the following conditions: microwave power = 0.998 mW, microwave frequency = 9.417 GHz, center field = 335.5 mT, modulation width = 0.2 mT, and modulation frequency = 100 kHz. PFRs were directly detected, whereas SO₄^{•−} and ¹O₂ were identified after exposure to BMPO and TEMP as the respective spin traps. BMPO that belongs to the category of a cyclic nitron spin trap popularly used for the EPR detection of •OH and superoxide radical was selected based on the previous finding [37] that it was more effective than 5,5-dimethyl-1-pyrroline N-oxide (DMPO) for the spin trapping of •OH and SO₄^{•−}.

2.4. Isothermal titration calorimetry (ITC) measurement

To explore the effect of thermal annealing on the surface affinities of the BCs, the association constant, K_b , for the interaction of a pristine or modified BC with PDS molecules was empirically estimated using ITC to quantify heat either released or absorbed as a result of the intermolecular binding. The ITC measurements were performed on a Nano ITC (TA Instruments) at 25 °C. Prior to the titrations, vacuum degasification was conducted for 20 min to eliminate air bubbles from the experimental suspensions. In each ITC run, 7 µL of 7.5 mM PDS was cyclically added 20 times at fixed intervals of 200 s between two successive injections into a 1-mL sample cell containing 0.05 g/L BC suspension continuously stirred at 250 rpm. The heat gain or loss caused by PDS binding to BC was determined after every PDS injection. It was estimated based on the power consumed to keep the temperature difference between reaction and reference cells (containing the BC suspension and distilled water, respectively) constant. The enthalpy change occurring while a BC suspension was diluted by multiple PDS injections (i.e., heat of dilution) was excluded from the binding isotherm, and the data were analyzed using a one-site model available in NanoAnalyze software (version 3.6.0).

3. Results and discussion

3.1. Persulfate activation capability of UKBRC biochars

UKBRC BCs, prepared by pyrolyzing the biomasses of six different origins at 550 and 700 °C, were tested for oxidative elimination of 4-CP as a model substrate (nonsusceptible to direct persulfate oxidation (*data not shown*)) in the presence of PMS and PDS (Fig. 1 and S1). Considering the extent of 4-CP removal by adsorption in dark (performed without persulfate addition), all tested BCs except for SS700 exhibited marginal carbocatalytic activities, regardless of the persulfate precursor type and

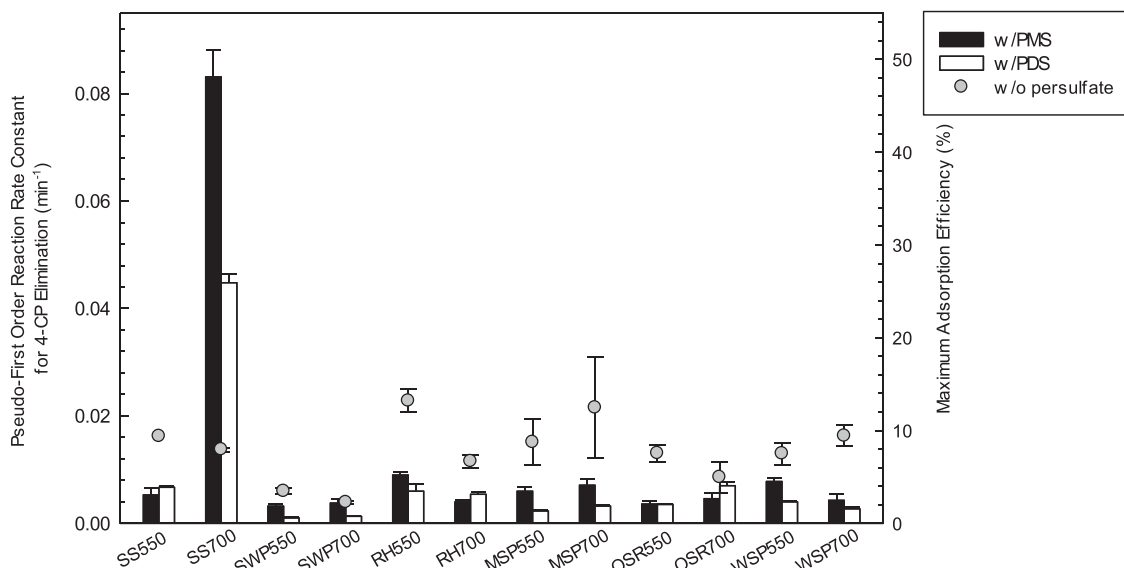


Fig. 1. Comparison of UKBRC BCs in terms of efficiencies of persulfate activation and adsorption ($[BC]_0 = 0.6$ g/L; $[4-CP]_0 = 0.1$ mM; $[PMS]_0 = [PDS]_0 = 1$ mM; $[phosphate\ buffer]_0 = 1$ mM; $pH_i = 7.0$).

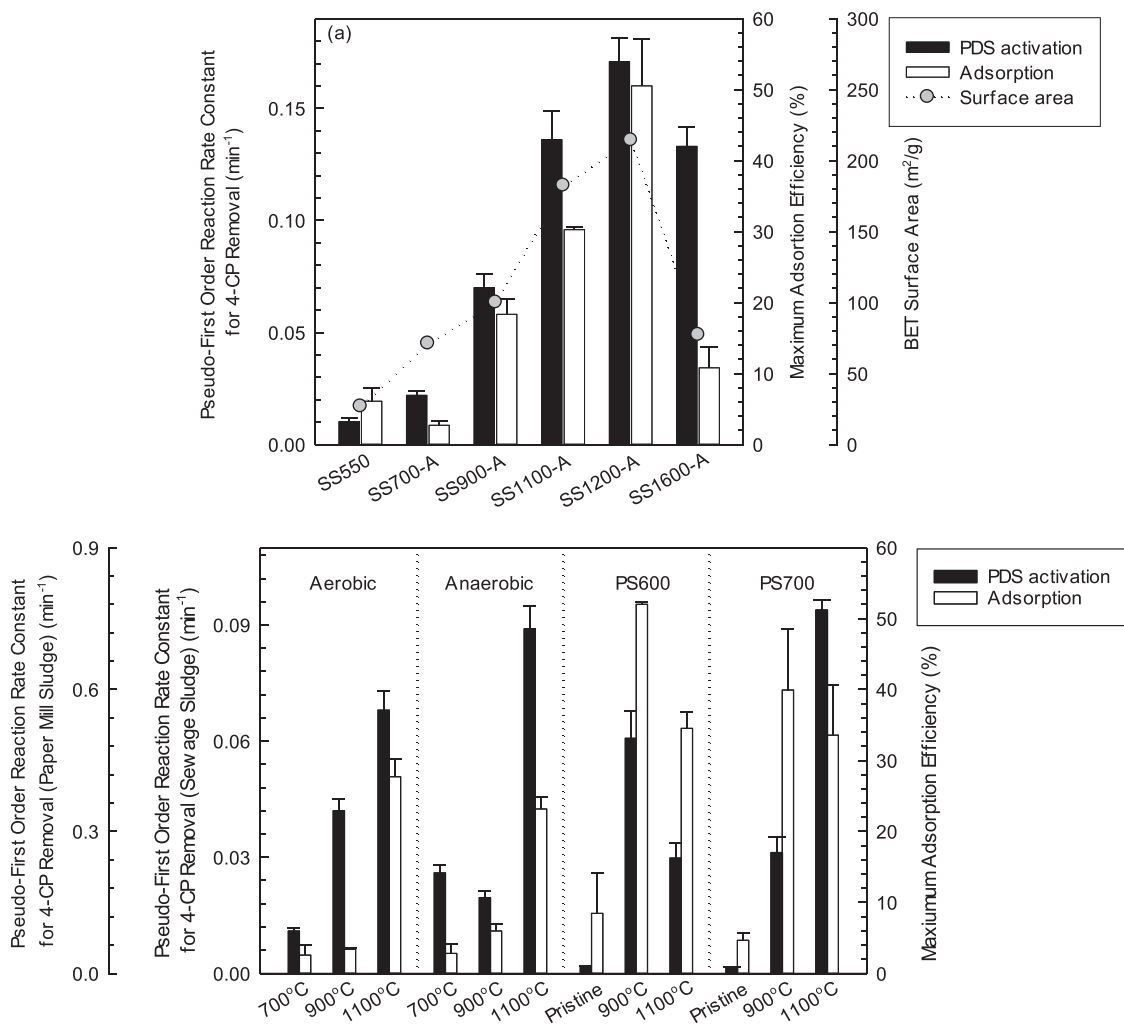


Fig. 2. Dependence of efficiencies of (a) UKBRC SS BCs and (b) aerobic/anaerobic sewage sludge- (AESS and ANSS) and paper mill sludge (PS)-derived BCs for PDS activation and adsorption on annealing temperature ($[BC]_0 = 0.1$ (PS600 and PS700 BCs) or 0.2 (SS, AESS, and ANSS BCs) g/L; $[4-CP]_0 = 0.1$ mM; $[PMS]_0 = [PDS]_0 = 1$ mM; $[phosphate\ buffer]_0 = 1$ mM; $pH_i = 7.0$).

the pyrolysis temperature. SS700 achieved the highest 4-CP degradation efficiency when either PMS or PDS was added. Although RH550, MSP700, and WSP550 selectively activated PMS, their catalytic activities, determined based on pseudo-first order reaction rate constants for 4-CP decomposition, were approximately tenfold lower than that of SS700. In particular, only the SS BCs exhibited markedly improved treatment performances with the pyrolysis temperature increasing from 550 to 700 °C, revealing that the beneficial effect of heat treatment on the persulfate activation capability was unique to them. Irrespective of the persulfate precursor used, SS700 exhibited a substantially faster 4-CP elimination than SS550, with $k(\text{SS550}) = 0.0053 \text{ min}^{-1}$ and $k(\text{SS700}) = 0.083 \text{ min}^{-1}$ under PMS addition and $k(\text{SS550}) = 0.0067 \text{ min}^{-1}$ and $k(\text{SS700}) = 0.044 \text{ min}^{-1}$ under PDS addition, respectively. In contrast, the carbocatalytic activities of the SWP and MSP BCs were insensitive to the variation in the pyrolysis temperature, and although RH550 and WSP550 outperformed RH700 and WSP700 in 4-CP removal on persulfate addition, the difference between their removal efficiencies was minimal.

3.2. Enhancing effect of thermal annealing

To examine the hypothesis that thermal annealing selectively improves the catalytic activities of the SS BCs, all BC550 samples were annealed at 1100 °C under anoxic conditions and the resultant products (BC1100-A, where "A" denotes annealing) were comparatively assessed in terms of PDS activation (Fig. S2). Aligned with the dependence of the catalytic activities of the BCs on the pyrolysis temperature (Fig. 1), annealing at 1100 °C caused a ca. 13-fold increase in the 4-CP elimination efficiency of SS550. This markedly contrasted with annealing barely promoting the performances of the other BCs. The enhancing effect of thermal treatment was further confirmed based on the pseudo-first order rate constant for 4-CP elimination by SS BC/PDS as a function of the annealing temperature (Fig. 2a and S3). The 4-CP removal efficiency was steadily improved as the annealing temperature increased up to 1200 °C and subsequently declined by a moderate extent on heat treatment at 1600 °C. This trend conformed to the temperature-dependent changes in the maximum adsorption efficiency (monitored after 4-CP was exposed to the SS BCs in the absence of PDS for 10 min) and the BET surface area. Elevating the pyrolysis temperature facilitated the carbon phase transformation and volatile substance release, increasing the surface areas of the BCs; however, their exposure to excess heat collapsed their porous structures, reducing the surface areas [13]. This suggests that the increased access to surface catalytic sites provided by the annealing of the SS BCs at higher temperatures could be a key to the observed beneficial effect of heat treatment. However, the finding that the surface areas of the other BCs (almost unreactive toward persulfate) were comparable to or higher than those of the annealed SS BCs (Table S1) suggested that another factor(s) may be involved in the temperature-sensitive carbocatalytic performances of the SS BCs. Furthermore, the contribution of the SS BC-activated persulfate became more pronounced on annealing up to 1600 °C because increasing the annealing temperature from 1200 to 1600 °C decreased the BET surface area by a factor of ca. 2.8. Specifically, $E_{\text{W/PDS}}/E_{\text{W/O PDS}}$ (where $E_{\text{W/PDS}}$ and $E_{\text{W/O PDS}}$ represent the 4-CP elimination efficiencies of the SS BCs in the presence and absence of PDS, respectively) was approximately 6.5, whereas these ratios for the other annealed SS BCs most ranged from 1.1 to 2.6. The ratios were determined based on the residual 4-CP concentrations monitored after a 10-min reaction.

3.3. Identification of key factors for catalytic activities of annealed biochars

To investigate the cause of the relation between the catalytic activity enhancement and annealing observed exclusively for the SS BC samples, select BCs (i.e., SS, RH, and SWP) prepared at 550 and 700 °C were characterized in terms of (i) defect density and graphitic carbon

concentration, (ii) surface functionality, (iii) chemical composition, and (iv) BET surface area (Fig. S4 and Tables S1 and S2). Comparison of the Raman spectral features of the SS, RH, and SWP BCs suggested a poor correlation of the defect density (or the graphitic carbon content) with the persulfate activation capacity (Fig. S4a). This is incompatible with previous studies reporting that modification strategies to create defective sites or increase the extent of graphitization can improve carbocatalytic activity [38,39]. For instance, increasing the pyrolysis temperature has been shown to reduce the intensity ratio of the D band at $\sim 1350 \text{ cm}^{-1}$ and the G band at $\sim 1585 \text{ cm}^{-1}$ ($I_{\text{D}}/I_{\text{G}}$), which are the respective quantitative indicators of defect and sp^2 carbon concentrations [40]. However, the difference between the persulfate activation efficiencies of RH550 and RH700 (or SWP550 and SWP700) was negligible. Furthermore, the change in the pyrolysis temperature drastically promoted the treatment efficiency of the SS BC/PDS, whereas SS550 and SS700 barely differed in terms of the $I_{\text{D}}/I_{\text{G}}$ values.

FT-IR spectra of the RH, SWP, and SS BC samples (Fig. S4b) indicated the presence of hydroxyl, carbonyl, and carboxylic moieties on the surfaces based on the peaks at 3425, 1610, and 1050 cm^{-1} attributed to the stretching vibrations of O-H, C=O, and C-O, respectively [41–43]. BC700 presented weaker IR peaks at 1050 and 781 cm^{-1} , indicating C-O and aromatic C-H moieties [42], than BC550 because pyrolysis at elevated temperatures ($> 700 \text{ °C}$) causes the reduction of oxygen functional groups and dehydration of aromatics [42]. By contrast, comparison of the peak intensities at 3425 and 1610 cm^{-1} of BC550 and BC700 implied that the surface hydroxyl and carbonyl groups remained intact as the pyrolysis temperature increased from 550 to 700 °C. Oxygen-containing functional groups contribute to promoting the efficiency of oxidizing radical production via persulfate activation [39,44]. Considering that a carbonyl moiety catalyzes persulfate decomposition with $^1\text{O}_2$ release [6,45], an increased surface density of oxygen functional groups could favor the generation of non-radical oxidant during BC-induced persulfate activation. However, in view of the minor difference between the RH, SWP, and SS BC samples in the type and concentration of oxygen functional groups, surface functionality was not a key factor for the PDS activation capabilities of the BCs. Furthermore, SS700 confirmed as the best-performing persulfate activator possessed a lower surface density of hydroxyl and carbonyl groups as reactive sites for carbocatalysis than SS550. The feasibility of heat treatment as an approach to increase the surface area [13] was confirmed to a certain extent based on the comparison of the BET surface areas of the BC samples prepared at 550 and 700 °C (Table S1). The S_{700}/S_{550} ratios (S_{700} and S_{550} denote the respective BET surface areas of BC550 and BC700) were determined as 0.9, 5.6, and 5.8 for the RH, SWP, and SS BCs, respectively. However, the marginal difference between SWP550 and SWP700 in terms of the persulfate activation efficiency suggested that the surface area increase was not necessarily accompanied with catalytic activity improvement. Furthermore, the surface area and PDS activation efficiency of the BC700 samples were poorly correlated (Fig. 1 and Table S1).

Based on EDS elemental analysis, the prominent feature distinguishing the SS BCs from the others was the surface chemical composition (i.e., low carbon and high mineral contents) (Tables S2 and S3). According to previous findings, the interaction between iron and carbon constituents at high temperatures leads to the concomitant formation of graphitic carbon and crystalline zerovalent iron [30,46–48] that serve as reactive sites for persulfate activation [24,30]. This suggests that among the inorganic constituents, the iron component, detected at a high content of ca. 9 % (high Fe/C ratio of ca. 20–30 %) in the SS BCs, could substantially improve their catalytic activities on thermal treatment. Specifically, endogenous iron in the carbon matrix could reductively transform into an elemental counterpart (i.e., carbothermal reduction), which in turn, could catalyze graphitization when iron-containing biomasses or chars are heat-treated. To explore the proposed role of iron species, aerobic and anaerobic SSs (AESS and ANSS, respectively) (collected from a sewage treatment plant in

Pyeongtaek, Gyeonggi Province, Korea) and paper mill sludge (PS) BCs were annealed at varying temperatures of 700, 900, and 1100 °C and the resultant carbon products were examined for PDS activation (Fig. 2b, S5, and S6). The measured iron contents of the pristine AESS, ANSS, PS600, and PS700 were 1.2 %, 2.7 %, 16.7 %, and 26.7 %, respectively. The carbocatalytic activities of all tested samples substantially increased in proportion to the annealing temperature in most cases, with $k(\text{AESS700}) = 0.011 \text{ min}^{-1}$ versus $k(\text{AESS1100}) = 0.068 \text{ min}^{-1}$ and $k(\text{PS700}) = 0.012 \text{ min}^{-1}$ versus $k(\text{PSS1100}) = 0.77 \text{ min}^{-1}$ (note that annealing scarcely improved the catalytic activities of most BC samples (except for the SS BCs) (Fig. S2)). These results support that the iron component is critical in boosting the persulfate activation capabilities of the BCs by thermal annealing.

3.4. Characterization of thermally annealed sewage sludge biochars

SEM images of the SS BCs thermally treated at varying temperatures showed that the annealed SS BCs were distinctive from the untreated counterpart (i.e., SS550) in terms of the morphological features. Superficially, smooth-surfaced particles began to appear at 700 °C, which subsequently agglomerated at higher annealing temperatures ranging from 1100 to 1600 °C, transforming into rod- and distorted sphere-shaped products with average sizes of ca. 0.05–0.5 μm (Fig. 3). The formation of micro-sized iron particles after thermal annealing, confirmed by the EDS elemental mapping (Fig. 3j–l), was unique to the SS BCs (note that similar morphological characteristics were not observed in the SEM images of the other BCs (Fig. S7)). In particular, in the TEM images of SS900-A, SS1100-A, and SS1600-A, iron microparticles were observed to be encapsulated by multilayered graphitic carbon shells (Fig. 3g–i and S8). These appeared to align with forming core-shell structures during high-temperature heat treatment of iron-

impregnated BCs [48,49] and producing carbon-encapsulated iron nanoparticles (NPs) in the iron-catalyzed graphitization process [46]. Transition metal cores, such as those of iron and nickel, increase the electron density of their outer carbon shells, kinetically enhancing the interfacial electron transfer to persulfate over the metal-carbon composites [50,51]. Accordingly, carbon-encapsulated iron particles, which were more frequently detected in the SS BCs with increasing temperature, are probable to serve as crucial reactive sites in persulfate activation by the annealed SS BCs.

According to previous findings, iron as a catalyst minimizes the heat energy required to convert non-graphitic carbon to graphitic carbon (i.e., catalytic graphitization) [46,52,53] and the progress of graphitization steadily improves the catalytic activities of carbon-based persulfate activators [8,24]. These suggest that thermal annealing could increase the content of graphitic carbon in the SS BCs, which could be responsible for the superiority of the heat-treated SS BCs to the other ones. Contrary to the hypothesis, the Raman spectra of a series of SS BCs heated with increasing annealing temperature revealed that iron-mediated graphitization barely occurred, with $I_D/I_G = 1.00, 0.98, 1.09, 1.14,$ and 1.11 for SS550, SS700-A, SS900-A, SS1100-A, and SS1200-A, respectively (Fig. 4a). However, the possibility of graphitization was not entirely eliminated based on the lattice fringes with interplanar spacings of 0.33–0.36 nm [54] observed in the TEM images of SS1100-A, SS1200-A, and SS1600-A (Fig. S8). Furthermore, the $sp^2\text{C}/sp^3\text{C}$ ratio, estimated by deconvolution of the C1s XPS spectra of the SS BCs, generally exhibited an increasing trend as SS550 was annealed at higher temperature (Figs. S9 and S10). The Raman spectral features of SS1600-A were clearly distinguished from those of the other SS BCs. Together with the lowest I_D/I_G (0.67), highest $sp^2\text{C}/sp^3\text{C}$ ratio (0.5), and inter-lattice spacing of 0.363 nm [54], the G band sharpening indicated the generation of highly crystalline graphitic carbon material [55], and a 2D band

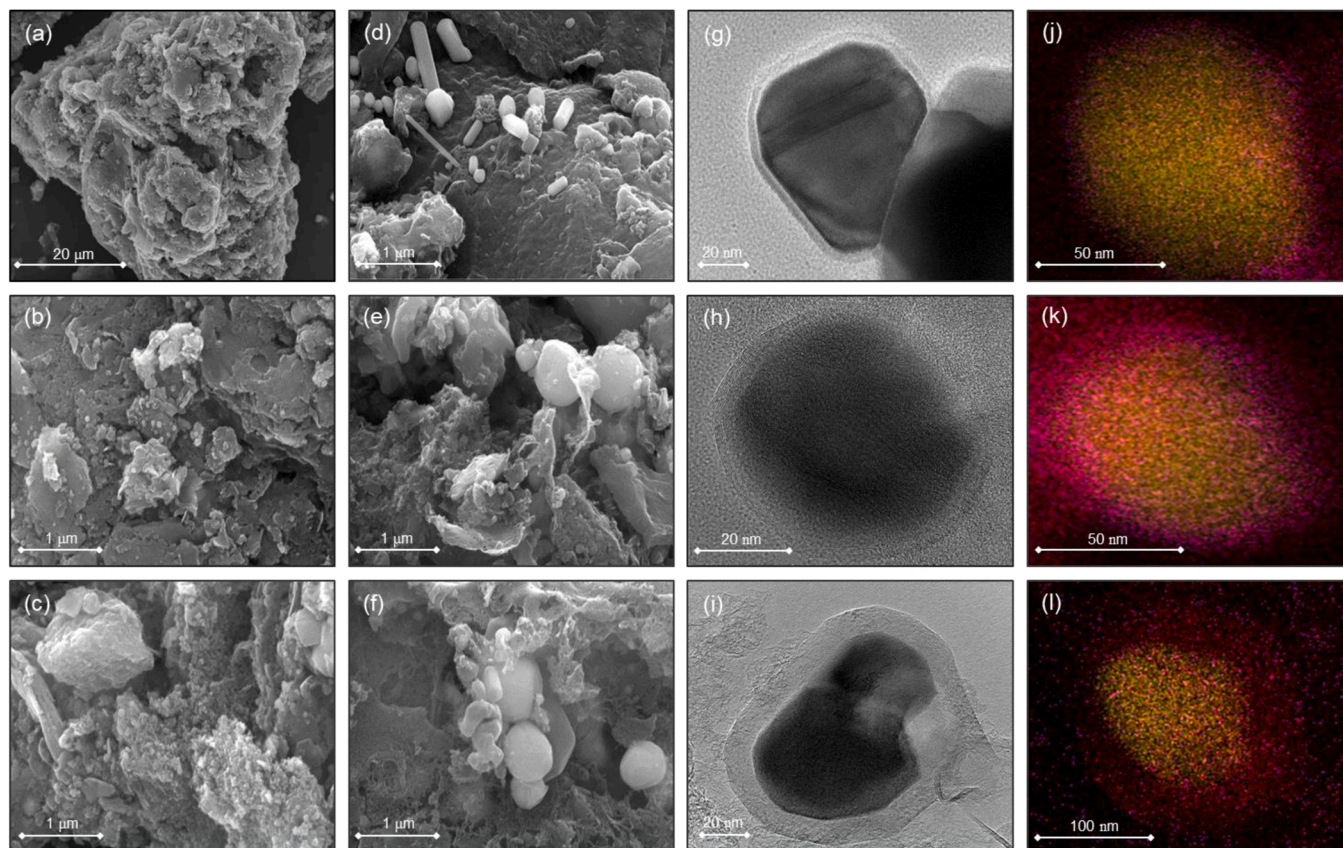


Fig. 3. SEM images of (a) SS550, (b) SS700-A, (c) SS900-A, (d) SS1100-A, (e) SS1200-A, and (f) SS1600-A and TEM images and EDS elemental maps of SS900-A ((g), (j)), SS1100-A ((h), (k)), and SS1600-A ((i), (l)), respectively. Yellow and red dots in elemental maps represent iron and carbon, respectively.

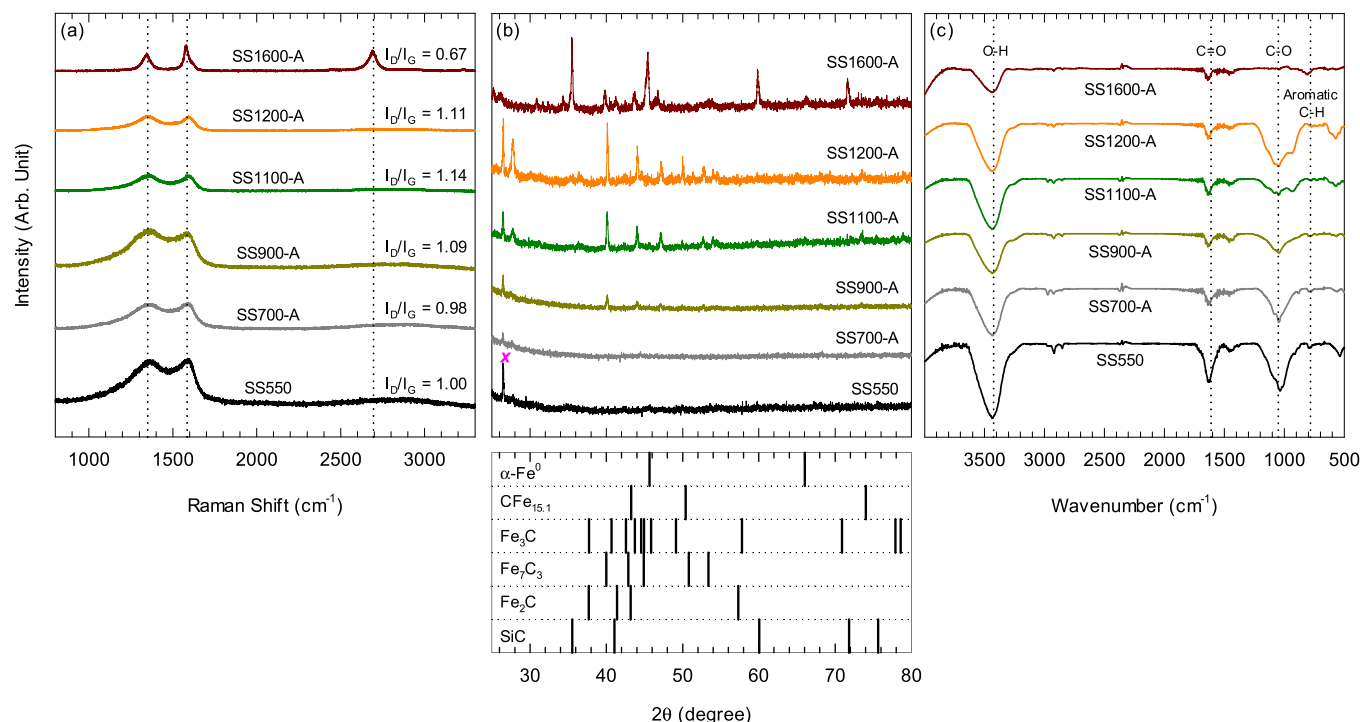


Fig. 4. (a) Raman spectra, (b) diffraction patterns, and (c) FT-IR spectra of annealed SS BCs.

at $\sim 2695\text{ cm}^{-1}$, associated with the double phonon scattering in graphene [56], newly emerged as an evidence of graphene formation. Carbon phase transformation related to the observation that annealing at 1600 °C significantly improved the catalytic performance of the SS BCs against the reduction in the sorption capacity and BET surface area (Fig. 2).

The temperature-dependent changes in the diffraction patterns of the SS BCs indicated that amorphous iron reductively transformed into zerovalent iron ($\alpha\text{-Fe}^0$) via iron carbide intermediates (i.e., Fe_2C , Fe_7C_3 , Fe_3C , and $\text{CFe}_{15.1}$) as the annealing temperature increased [48,57] (Fig. 4b). The major peaks at 2θ of approximately 45 and 66°, which were indexed to the (110) and (200) planes of $\alpha\text{-Fe}^0$, respectively [48], were observed exclusively for SS1600-A, whereas diffraction features indicating iron carbide formation appeared in the temperature range of 900–1200 °C and vanished at 1600 °C. These results align with the crystal lattice fringes with the interplanar distance of 0.2 nm corresponding to the lattice spacing of the (110) plane of $\alpha\text{-Fe}^0$ [58] observed in the TEM image of SS1600-A (Fig. S8d). In particular, the conversion of crystalline silica (confirmed by the characteristic peak at $2\theta = 26.2$ [59]) into silicon carbide (SiC) was unique to SS1600-A, supporting the reductive Fe^0 formation in the carbon matrix at 1600 °C (note that the carbothermal reduction in silica/charcoal (leading to SiC occurrence) proceeds at 1600 °C or higher [60]). Fe_3C and Fe^0 formed during the calcination of iron-polymer mixtures have been shown to enable effective PDS activation by carbon-encapsulated iron NPs [61], and Fe^0 has been reported to be superior to Fe_3C in the catalytic reductive conversion by iron/BC composites [48]. Considering these, in this study, the temperature-sensitive variation in iron speciation was related to the beneficial effect of thermal annealing on the catalytic activities of the SS BCs (Fig. 2a). The role of the iron component in promoting the performances of the SS BCs by annealing was confirmed by acid washing of the SS BCs for iron extraction. The diffraction pattern of SS1100-AR-A, prepared by thermal annealing at 1100 °C after exposure of SS550 to 1N aqua regia, indicated marginal formation of Fe^0 and iron carbides due to the significant iron loss by the acid pre-treatment (Fig. S11a). The iron content was reduced to approximately 0.48 % based on the EDS elemental map, and the morphology of an iron core/carbon shell

structure was not observed in the TEM image of SS1100-AR-A (Fig. S12). In contrast, SS1100-A-HCl, formed by sequential application of acid washing (with 1N HCl) followed by annealing, retained Fe^0 and iron carbides (Fig. S11a). This was ascribed to the carbon encapsulation occurring on heat treatment protecting the iron-based core from acid-induced extraction. SS1100-AR-A still achieved higher PDS activation efficiency than the unmodified SS550, whereas SS1100-A-HCl achieved an approximately fourfold faster 4-CP elimination than SS1100-AR-A in the presence of PDS (Fig. S11b). Thermal annealing pronouncedly enhanced the adsorption and PDS activation capability of SS1100-A-HCl, which barely lost iron on post-treatment with HCl.

The FT-IR spectrum of pristine SS550 comprised three primary characteristic peaks assigned to -OH , C=O , and C-O groups (Fig. 4c). In accordance with the influence of heat treatment on the surface functionalities of the BCs, increasing the annealing temperature gradually decreased the intensities of all detected IR peaks, suggesting that post-heat treatment eliminated chemical moieties on the BC surfaces. The removal of oxygen functional groups by annealing was also confirmed by the C1s spectra of the pristine and thermally treated SS BCs (Figs. S9 and S10). Because the SS BCs annealed at higher temperatures performed more effective persulfate activation (Fig. 2a), the type and surface density of functional groups were not associated with the enhancing effect of annealing, though select oxygen-containing groups such as -OH and C=O were reported to facilitate the production of radical and non-radical oxidants through one-electron reduction and self-decomposition of persulfate [6,39,44,45]. This was supported based on the performance testing of acid-treated SS BCs (prepared by washing SS700 with 1N HCl, HNO_3 , H_2SO_4 , and aqua regia). The 4-CP degradation efficiencies by PDS activation increased in the following order: SS700 (aqua regia) < SS700 (HNO_3) < SS700 (H_2SO_4) < SS700 (HCl) (Fig. S13). In the FT-IR spectra of the acid-treated SS samples, oxygen-containing functional groups were scarcely detected on the SS700 (HCl) surface, suggesting their loss, whereas the IR peaks assigned to C=O and C-O moieties remained intact or became more pronounced for the other samples (Fig. S14a). The peak at 1383 cm^{-1} indicative of C-H bending vibration commonly appeared after acid washing. Note that among the acid-treated SS BCs, SS700 (HCl) contained the relatively abundant

graphitic carbon (lowest I_D/I_G of 0.87) and iron, as confirmed by Raman spectroscopy and EDS elemental analysis (Fig. S14b and Table S3).

3.5. Factors improving catalytic activity by annealing

To explore the impact of thermal annealing on the electron transfer-mediating capabilities of the SS BCs (presumed as being crucial in persulfate activation [3,62]), temporal variations in the OCPs of SS550/FTO, SS700-A/FTO, SS900-A/FTO, SS1100-A/FTO, SS1200-A/FTO, and SS1600-A/FTO as working electrodes were recorded. In these measurement, PDS and 4-CP serving as the electron acceptor and donor, respectively, were sequentially injected (Fig. 5a). Regardless of the type of the SS BC, the addition of PDS and 4-CP caused OCP shifts in positive and negative directions, respectively, which confirmed their roles in carbocatalytic activation by the SS BCs. The positive and negative shifts indicated electron flow from the SS BC to

PDS and from 4-CP to the SS BC, respectively [63]. Marginal OCP shifts observed with SS550/FTO conformed to the low catalytic activity of SS550 for PDS activation. The OCP shifts in the response to PDS and 4-CP injections became more significant with increasing annealing temperature in most cases. The extents of the positive and negative OCP shifts increased in the following order: SS700-A < SS900-A < SS1100-A \approx SS1200-A \approx SS1600-A. This order suggests that the high catalytic activities of the thermally treated SS BCs were ascribed to the improvement of the electron transfer-mediating capacity by annealing as a post-treatment step.

The dependence of the binding affinities of the SS BCs to PDS on annealing was investigated based on the magnitude of the binding constant, K_b , extracted from ITC-derived thermodynamic parameters (e. g., enthalpy and entropy) associated with the interactions between the SS BCs and PDS molecules (Fig. 5b and Table S4). Raising the annealing temperature from 550 to 900 °C gradually increased K_b ; however,

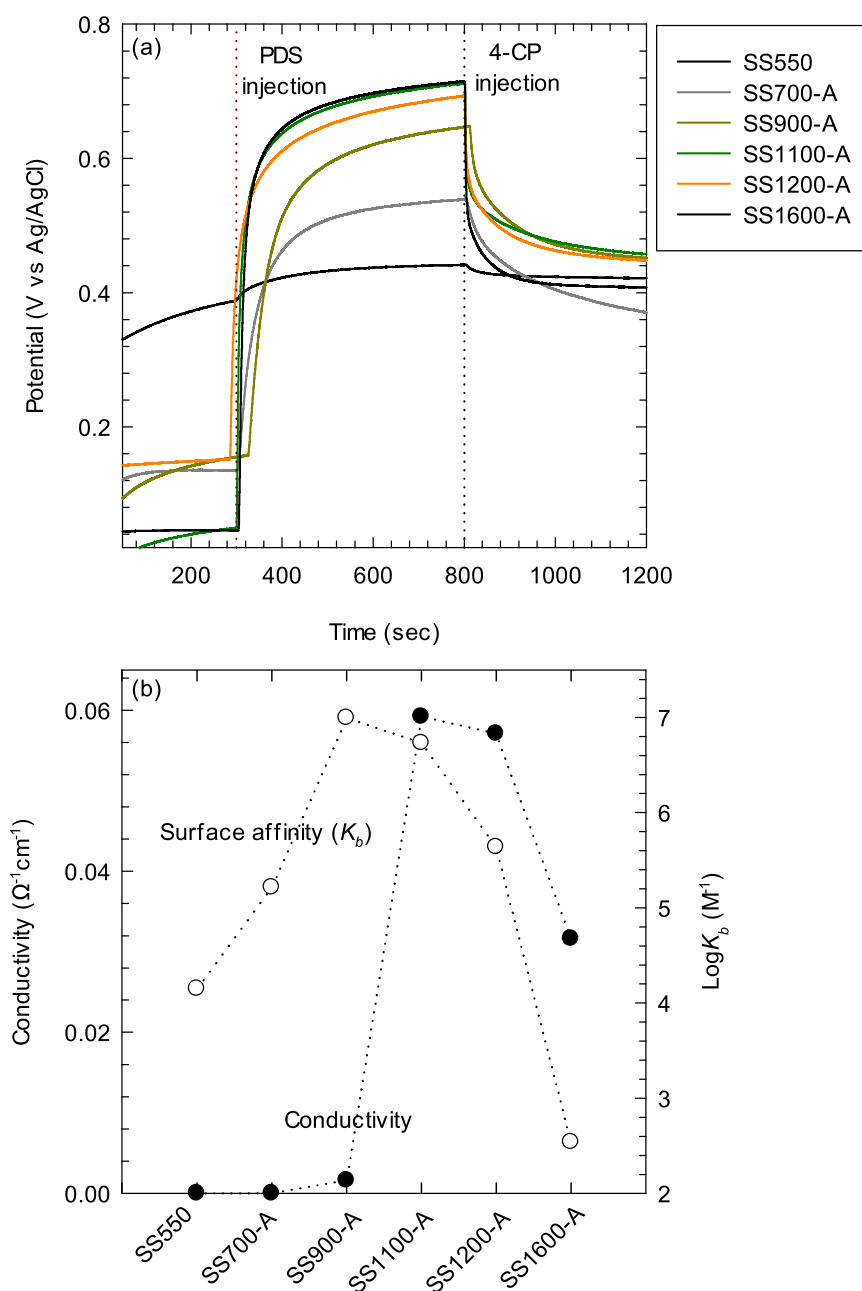


Fig. 5. (a) Changes in OCPs of annealed SS BC-coated FTO electrodes in response to addition of PDS and 4-CP and (b) variations in binding energy (K_b) and electrical conductivity of SS BCs with annealing temperature.

further temperature increase led to a steady decline in the binding affinity. A volcano-type dependence aligned with the sorption capacity (or the BET surface area) of the annealed SS BCs as a function of the annealing temperature to a certain extent (Fig. 2a). Thus, the surface affinities of the SS BCs, which were modifiable by the annealing temperature, could be expected to be a determinant of the overall treatment performances of the SS BC/PDS systems. However, it was observed that SS1600-A, whose K_b was approximately four orders of magnitude lower than that of SS900-A, outperformed the other annealed SS BCs in persulfate activation. This suggested that the electron transfer-mediating capacity was the overriding factor in the carbocatalytic activities of the annealed BCs. This was supported by the electrical conductivities of the SS BCs prepared at varying annealing temperatures (Fig. 5b) as well as the OCP shifts of the annealed SS BCs (Fig. 5a). Specifically, thermal treatment of the SS BCs at temperatures above 900 °C caused a drastic improvement in the electrical conductivity. Zeta potentials of the heat-treated SS BCs as functions of pH showed that SS1600-A induced an electrostatic attraction with anionic PDS under acidic and neutral conditions (Fig. S15). By contrast, the other SS BCs exhibited negative

surface charges over a wide pH range of 4–11. This may additionally contribute to the excellence of SS1600-A as a persulfate activator.

PFRs have been presumed to result from (i) the homolytic dissociation of chemical bonds (e.g., C-O and C-C) in biomass and (ii) the electron transfer from biomass-derived phenol and (hydro)quinone moieties to transition metals (either inherent in biomass or externally added) during pyrolysis for BC production [16,64]. Semiquinone- and phenoxyl-type PFRs exhibit natural lifespans of days to months owing to resonance stabilization and can generate reactive oxygen species by transferring electrons to oxygen and peroxides [16,65]. Based on the previously reported nature of PFRs as reactive sites in the reductive transformation of persulfate into $\text{SO}_4^{\cdot-}$ [16,66], we explored the quantitative relation between the PDS activation performances of the BCs and the intensity of the singlet EPR signal in the magnetic fields of 334–338 mT (assigned to PFRs) (Fig. S16). However, no correlation was observed; MSP550, SWP550, and OSR550 with the relatively high EPR peaks barely activated PDS, and SS700, which outperformed the other BC700 samples in PDS activation, exhibited nearly no EPR spectral features. Moreover, EPR signals were not detected for the annealed SS BCs. The

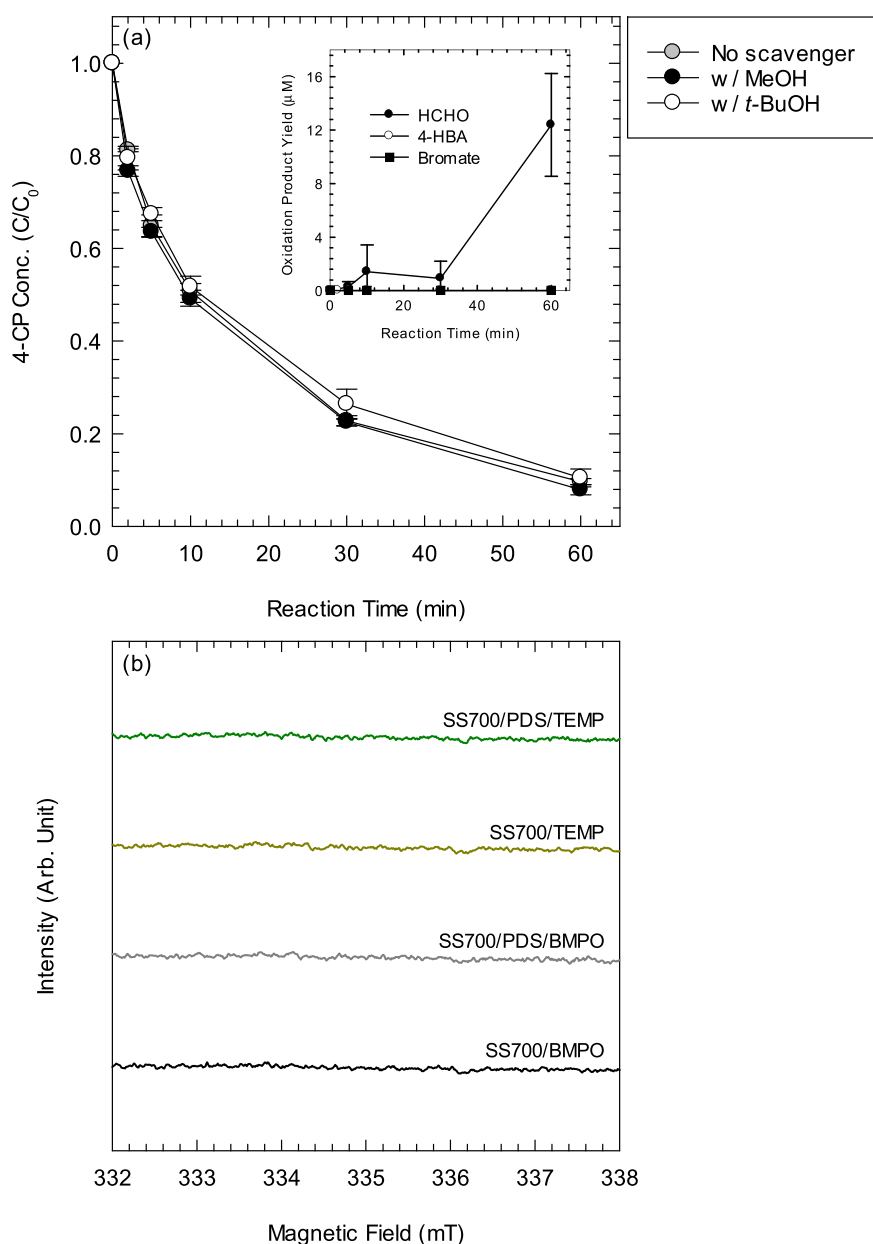


Fig. 6. (a) 4-CP removal by SS700/PDS in presence of alcohol-based scavengers ($[\text{BC}]_0 = 0.1 \text{ g/L}$; $[\text{4-CP}]_0 = 0.1 \text{ mM}$; $[\text{PDS}]_0 = 1 \text{ mM}$; $[\text{alcohol}]_0 = 0.2 \text{ M}$; $[\text{phosphate buffer}]_0 = 1 \text{ mM}$; $\text{pH}_i = 7.0$) and (b) EPR spectra of SS700 alone and SS700/PDS mixtures in presence of BMPO and TEMP as spin traps ($[\text{BC}]_0 = 0.2 \text{ g/L}$; $[\text{PDS}]_0 = 1 \text{ mM}$; $[\text{BMPO}]_0 = 1 \text{ mM}$; $[\text{TEMP}]_0 = 10 \text{ mM}$; $[\text{phosphate buffer}]_0 = 1 \text{ mM}$; $\text{pH}_i = 7.0$). Inset shows HCHO, 4-HBA, and BrO_3^- formation ($[\text{BC}]_0 = 0.6 \text{ g/L}$; $[\text{PDS}]_0 = 1 \text{ mM}$; $[\text{MeOH}]_0 = 0.2 \text{ M}$; $[\text{Br}^-]_0 = 0.1 \text{ mM}$; $[\text{BA}]_0 = 10 \text{ mM}$; $[\text{phosphate buffer}]_0 = 1 \text{ mM}$; $\text{pH}_i = 7.0$).

results revealed that the observed organic degradation by BC-activated PDS did not rely on oxidative attacks by radicals such as $\text{SO}_4^{\bullet-}$.

3.6. Major degradative reaction routes

According to the LC-MS identification of intermediates generated during 4-CP oxidation by SS700-activated PDS (Table S5), the temporal loss of 4-CP observed during PDS activation resulted from its oxidative degradation. Intermediates included hydroquinone, 2-chloro-3-hydroxybenzoic acid, and 4-chloro-5-hydroxy-1,2-benzoquinone (via hydroxylation reaction), 2-(naphthalen-2-yl)-2-oxoacetic acid (via coupling reaction), and maleic acid (via ring-opening reaction). Different from the role of the iron component in the BCs in initiating one-electron persulfate reduction (leading to $\text{SO}_4^{\bullet-}$) [49], the progress of non-radical PDS activation by the SS BCs was supported based on multiple empirical evidences. For instance, adding excess MeOH and *t*-BuOH, which acted as scavengers of $\bullet\text{OH}/\text{SO}_4^{\bullet-}$ and $\text{SO}_4^{\bullet-}$, respectively, barely decelerated 4-CP degradation by SS700/PDS (Fig. 6a). PDS activation in the presence of excess MeOH, Br^- , and BA led to negligible formation of HCHO, BrO_3^- , and 4-HBA as oxidation products (inset of Fig. 6a) that typically form via hydrogen atom-abstraction [67], electron

abstraction [68], and hydroxylation reactions [69] involving $\bullet\text{OH}$ and $\text{SO}_4^{\bullet-}$, respectively. The occurrence of $^1\text{O}_2$ as a non-radical oxidant, previously reported to form during persulfate activation by BCs [49], was eliminated based on the response of the FFA decay rate to solvent exchange from H_2O to D_2O (Fig. S17). The degradation of FFA as an indicator of singlet oxygenation by the annealed SS BC/PDS negligibly proceeded on the addition of D_2O , which extends the lifetime of $^1\text{O}_2$ by a factor of ten [70]. Absence of $\bullet\text{OH}/\text{SO}_4^{\bullet-}$ and $^1\text{O}_2$ formation was further corroborated by the EPR spectra features monitored in the presence of BMPO and TEMP as the spin traps of radical and non-radical oxidants, respectively. Specifically, no EPR peaks characteristic of $\bullet\text{OH}/\text{SO}_4^{\bullet-}$ and $^1\text{O}_2$ were detected during PDS activation by SS700 (Fig. 6b).

Together with the positive correlation between the electron transfer-mediating capacity and the catalytic activity for PDS activation (Figs. 2a and 5a), the substrate-specific reactivity of SS700/PDS (Fig. 7a and S18) implied the progress of mediated electron transfer as a non-radical pathway for persulfate activation, in which the SS700 carbocatalyst facilitated the transfer of electrons from organic contaminant, acting as an electron donor to PDS, serving as an electron acceptor. ACT and TCP rapidly decomposed, BPA, 4-CP, and PH underwent oxidation at moderate rates, and CBZ, NB, and BA were scarcely treated. Aligned with the

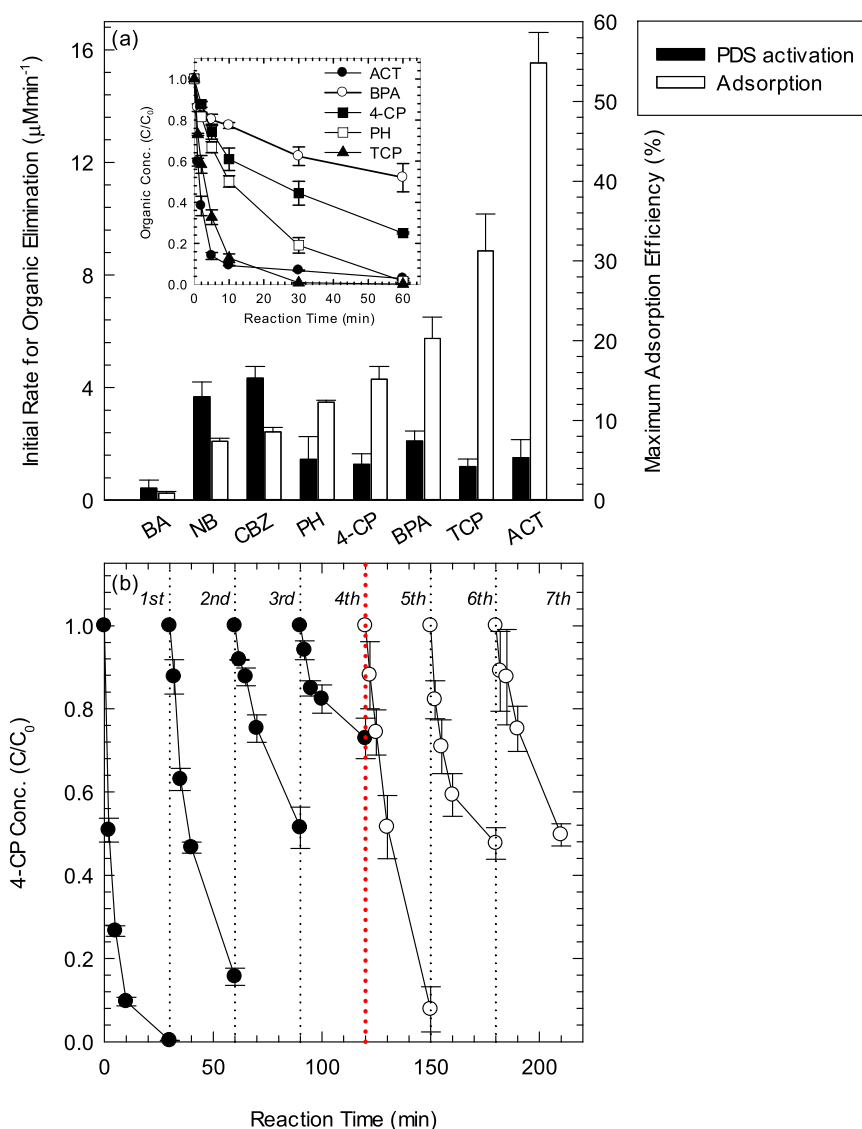


Fig. 7. (a) Removal of diverse organic compounds by SS700 and SS1100-A (inset) in absence and presence of PDS ($[\text{BC}]_0 = 0.2$ (SS1100-A) or 0.6 (SS700) g/L; $[\text{organic compound}]_0 = 0.1$ mM; $[\text{PDS}]_0 = 1$ mM; $[\text{phosphate buffer}]_0 = 1$ mM; $\text{pH}_i = 7.0$) and (b) repeated elimination of 4-CP by SS1100-A/PDS ($[\text{BC}]_0 = 0.2$ g/L; $[\text{4-CP}]_0 = 0.05$ mM; $[\text{PDS}]_0 = 1$ mM; $[\text{phosphate buffer}]_0 = 1$ mM; $\text{pH}_i = 7.0$). Red dotted line in Fig. 7b represents thermal treatment of used BC for regeneration.

selective nature of SS700/PDS, performance testing of SS1100-A showed higher susceptibility of ACT and TCP to persulfate oxidation than that of the other phenolic compounds such as PH, 4-CP, and BPA and significantly slow progress of BA, NB, and CBZ decomposition (inset of Fig. 7a and Fig. S19). This indicated that the BC modification by heat treatment did not alter the major degradation pathway for persulfate activation, which was plausible because thermally induced interaction between endogenous iron and carbon components should occur during the pyrolytic conversion of iron-containing sewage sludge into SS700. LC-MS and GC-MS analyses of the intermediates of 4-CP oxidation showed that hydroxylation, coupling, and ring-opening reactions mediated by SS1100-A/PDS yielded 4-chlorocatechol, 5-chloro-2,4-dihydroxybiphenyl, and 2-propenal/ethyl formate, respectively (Tables S6-7). The common occurrence of some intermediates, such as hydroquinone, 2-chloro-3-hydroxybenzoic acid, and 2-(naphthalen-2-yl)-2-oxoacetic acid, also confirmed the similarity in the primary degradative route between SS700/PDS and SS1100-A/PDS. Moreover, 4-CP removal by SS1100-A/PDS was not kinetically retarded in excess alcohol-based radical scavengers, and oxidative transformations of MeOH-to-HCHO, BA-to-4-HBA, and Br^- -to- BrO_3^- marginally proceeded during PDS activation. EPR spectral features corresponding to the formation of $\cdot\text{OH}/\text{SO}_4^{\cdot-}$ and $^1\text{O}_2$ were not observed for SS1100-A (Fig. S20), and the minor FFA decay in the presence of D_2O excluded the possible contribution of singlet oxygenation as the degradative pathway (Fig. S17).

The previous persulfate studies have presented the conflicting views regarding the primary degradative pathway(s) in the heterogeneous persulfate activation by iron-modified BCs [33–35,71]. For instance, $\text{SO}_4^{\cdot-}$ presumed to form via heterolytic cleavage of a peroxide bond in persulfate served as the major oxidant during persulfate activation by zerovalent iron/BC [71]. However, based on the moderate kinetic inhibition at excess alcohol-based radical scavengers and EPR detection, organics decomposed by iron/BC composites through non-radical persulfate oxidation involving $^1\text{O}_2$, high-valent iron, and mediated electron transfer [33–35]. To explore the reason behind the contradictory conclusions regarding the role of iron components in persulfate activation, the Fe/SWP samples prepared via iron-impregnation of SWP550 confirmed to be inert toward persulfate activation even after post-annealing at 1100 °C (Fig. S2) (details in Fe/SWP preparation are described in the caption of Fig. S21 [35]) were examined for 4-CP degradation in the presence of PDS under acidic and neutral conditions (Fig. S22). Aligned with the previous reports regarding the role of iron in promoting the catalytic activity of BCs in different ways [33–35, 71], the efficiency of Fe/SWP for 4-CP oxidation being steadily improved with increasing iron content indicated the involvement of iron components (having low-crystalline Fe_3C according to the diffraction patterns in Fig. S21) in PDS activation. The Fe sample primarily consisting of Fe_3O_4 was unreactive toward PDS. No regarding effect of MeOH, observed regardless of pH, likely suggested the occurrence of non-radical persulfate activation (Fig. S22). However, it is noteworthy that BA known to be highly resistant to non-radical persulfate oxidation [8,26] noticeably decomposed, which revealed the possibility that $\text{SO}_4^{\cdot-}$ bound to hydrophobic BC surface, which is not prone to scavenging by hydrophilic alcohol-based radical quenchers [72], acted as the secondary oxidant. Note that acidic condition often chosen for Fenton-like oxidation relying on peroxide-derived radicals favored BA degradation, which contrasted with the slower progress of 4-CP degradation at pH 3. The mechanisms for persulfate activation by the iron/BC composites should vary sensitively depending on the oxidation state of iron component, defect density of carbon phase, type of persulfate precursor, and composite configuration. Accordingly, in-depth further studies are required to unveil the key factors determining the main degradative pathway(s) during persulfate activation by iron-containing or iron-modified BCs.

3.7. Catalytic performance

Removal of 4-CP by SS1100-A/PDS led to significant TOC reduction but marginal CO_2 evolution (Fig. S23), suggesting that organic intermediates formed by the persulfate oxidation of 4-CP accumulated on the BC surface instead of mineralizing to CO_2 and H_2O . Note that thermal treatment promoted the sorption capabilities of the SS BCs (Figs. 2a and 5b). These intermediates adsorbed on the BC-based activator were expected to block surface reactive sites, causing catalyst deactivation. Reflecting this, the efficiency of SS1100-A/PDS for 4-CP elimination gradually decreased with increasing catalytic cycle when a repetition test was performed in the same batch. Specifically, 4-CP was periodically injected without spent solvent or catalyst exchange with fresh one (Fig. 7b). The 4-CP removal efficiency was reduced by approximately 20 % per each cycle. However, heat treatment at 500 °C under anoxic conditions recovered the catalytic activity of the spent SS1100-A to a marked extent; therefore, the 4-CP removal efficiency of the thermally regenerated SS1100-A was approximately 90 % of that of the pristine virgin counterpart. The SEM images of the used and regenerated SS1100-A samples showed that both retained the morphological features corresponding to carbon-wrapped iron particles commonly observed with the thermally annealed SS BCs, although carbon-encapsulated iron particles seemed to more densely cover the BC surface (Fig. S24). Further, the comparison among the fresh, used and regenerated SS1100-A samples in terms of the diffraction patterns implied that the iron carbides remained intact after the multiple use in PDS activation and thermal regeneration (Fig. S25). Therefore, the results reconfirmed that the observed steady reduction of the PDS activation efficiency resulted from the coverage of active surface sites by organic intermediates and anoxic annealing adopted as the catalyst reactivation strategy effectively removed surface-bound organics. The minor variation in the oxidation state of iron after repeated use supported that iron components promoted the electron-transfer mediation over the thermally annealed SS BCs by increasing the electron density of carbon shells (rather than serving as the redox active sites in directly inducing the one-electron reduction of persulfate often observed in the Fenton-like oxidation).

4. Conclusion

In this study, we explored the role of iron, which is frequently detected as a mineral component in biomasses, in fabricating and modifying BC-based carbocatalysts for persulfate activation via thermal treatment based on the comparative assessments using UKBRC BCs of different origins prepared at 550 and 700 °C. SS BCs outperformed the other UKBRC BCs in PDS activation and the gradual improvement of catalytic activity with increasing annealing temperature was unique to the iron-containing sewage and paper mill sludge-derived BCs (e.g., SS, AESS, and PS BCs). In addition to a marked increase in the BET surface area, the enhancing effect of annealing was associated with the formation of carbon-encapsulated iron particles on the SS BC surfaces, which became more pronounced as the pristine SS BC was annealed at higher temperatures. As confirmed by HR-TEM, XRD, Raman, and XPS analyses, heat-induced interaction occurred between the iron and carbon components (i.e., iron-catalyzed graphitization and carbothermal reduction) in the SS BCs. This led to the production of elemental iron and iron carbides and sp^3 -to- sp^2 transformation in the carbon phase. The modification of SS550 by heat treatment improved the electron transfer-mediating capacity and surface affinity toward PDS, and their temperature-dependent variations accorded with the catalytic performance of the SS BC, which increased in proportion to the annealing temperature. However, a comparative study of annealed and acid-washed SS BCs suggested a poor correlation between the surface densities of oxygen functional groups and the persulfate activation efficiency. The enhanced capabilities of the heat-treated SS BCs to mediate the transfer of electrons from organics to persulfate was responsible for

oxidative organic treatment based on the (i) marginal kinetic retardation in excess alcohol-based radical scavengers, (ii) OCP shifts on 4-CP and PDS addition, (iii) no EPR detection of radical and non-radical oxidants, and (iv) substrate specificity of organic elimination efficiency.

CRedit authorship contribution statement

Sae-In Suh: Investigation, Validation, Writing - Original Draft; **Heesoo Woo:** Investigation, Validation, Methodology; **So-Yeon Song:** Investigation, Methodology; **Dongjoo Park:** Methodology; **Yong-Yoon Ahn:** Methodology; **Eun-Ju Kim:** Methodology; **Hongshin Lee:** Conceptualization, Investigation; **Dong-Wan Kim:** Investigation, Validation; **Changha Lee:** Writing - Revised Manuscript; **Yong Sik Ok:** Conceptualization, Validation, Writing - Original Draft; **Jaesang Lee:** Conceptualization, Formal Analysis, Writing - Original Draft and Revised Manuscript.

Declaration of Competing Interest

The authors declare that they have no known competing financial interests or personal relationships that could have appeared to influence the work reported in this paper.

Data Availability

Data will be made available on request.

Acknowledgments

This study was supported by a National Research Foundation of Korea grant funded by the Korean government (grant no. 2021R1A2C2003763) and the Korea Ministry of Environment (grant no. RE202201829) and Korea Environment Industry and Technology Institute (KEITI) through the Developing Innovative Drinking Water and Wastewater Technologies Project (2022002710001).

Appendix A. Supporting information

Supplementary data associated with this article can be found in the online version at [doi:10.1016/j.apcatb.2023.122647](https://doi.org/10.1016/j.apcatb.2023.122647).

References

- [1] X.G. Duan, H.Q. Sun, S.B. Wang, Metal-free carbocatalysis in advanced oxidation reactions, *Acc. Chem. Res.* 51 (2018) 678–687, <https://doi.org/10.1021/acs.accounts.7b00535>.
- [2] W.Q. Huang, S. Xiao, H. Zhong, M. Yan, X. Yang, Activation of persulfates by carbonaceous materials: a review, *Chem. Eng. J.* 418 (2021), 129297, <https://doi.org/10.1016/j.cej.2021.129297>.
- [3] J. Lee, U. von Gunten, J.H. Kim, Persulfate-based advanced oxidation: critical assessment of opportunities and roadblocks, *Environ. Sci. Technol.* 54 (2020) 3064–3081, <https://doi.org/10.1021/acs.est.9b07082>.
- [4] H.Q. Sun, C. Kwan, A. Suvorova, H.M. Ang, M.O. Tade, S.B. Wang, Catalytic oxidation of organic pollutants on pristine and surface nitrogen-modified carbon nanotubes with sulfate radicals, *Appl. Catal. B Environ.* 154 (2014) 134–141, <https://doi.org/10.1016/j.apcatb.2014.02.012>.
- [5] X.G. Duan, H.Q. Sun, J. Kang, Y.X. Wang, S. Indrawirawan, S.B. Wang, Insights into heterogeneous catalysis of persulfate activation on dimensional-structured nanocarbons, *ACS Catal.* 5 (2015) 4629–4636, <https://doi.org/10.1021/acscatal.5b00774>.
- [6] X. Cheng, H.G. Guo, Y.L. Zhang, X. Wu, Y. Liu, Non-photochemical production of singlet oxygen via activation of persulfate by carbon nanotubes, *Wat. Res.* 113 (2017) 80–88, <https://doi.org/10.1016/j.watres.2017.02.016>.
- [7] E.T. Yun, J.H. Lee, J. Kim, H.D. Park, J. Lee, Identifying the nonradical mechanism in the peroxymonosulfate activation process: Singlet oxygenation versus mediated electron transfer, *Environ. Sci. Technol.* 52 (2018) 7032–7042, <https://doi.org/10.1021/acs.est.8b00959>.
- [8] B.W. Yang, H.S. Kang, Y.J. Ko, H. Woo, G. Gim, J. Choi, J. Kim, K. Cho, E.J. Kim, S. G. Lee, H. Lee, J. Lee, Persulfate activation by nanodiamond-derived carbon onions: Effect of phase transformation of the inner diamond core on reaction kinetics and mechanisms, *Appl. Catal. B Environ.* 293 (2021), 120205, <https://doi.org/10.1016/j.apcatb.2021.120205>.
- [9] H.Q. Sun, S.Z. Liu, G.L. Zhou, H.M. Ang, M.O. Tade, S.B. Wang, Reduced graphene oxide for catalytic oxidation of aqueous organic pollutants, *ACS Appl. Mater. Inter.* 4 (2012) 5466–5471, <https://doi.org/10.1021/am301372d>.
- [10] Y.L. Zhao, X.Z. Yuan, X.D. Li, L.B. Jiang, H. Wang, Burgeoning prospects of biochar and its composite in persulfate-advanced oxidation process, *J. Hazard. Mater.* 409 (2021), 124893, <https://doi.org/10.1016/j.jhazmat.2020.124893>.
- [11] Y.X. Qin, G.Y. Li, Y.P. Gao, L.Z. Zhang, Y.S. Ok, T.C. An, Persistent free radicals in carbon-based materials on transformation of refractory organic contaminants (ROCs) in water: a critical review, *Wat. Res.* 137 (2018) 130–143, <https://doi.org/10.1016/j.watres.2018.03.012>.
- [12] A. Tomczyk, Z. Sokolowska, P. Boguta, Biochar physicochemical properties: pyrolysis temperature and feedstock kind effects, *Rev. Environ. Sci. Bio* 19 (2020) 191–215, <https://doi.org/10.1007/s11157-020-09523-3>.
- [13] L.J. Leng, Q. Xiong, L.H. Yang, H. Li, Y.Y. Zhou, W.J. Zhang, S.J. Jiang, H.L. Li, H. J. Huang, An overview on engineering the surface area and porosity of biochar, *Sci. Total Environ.* 763 (2021), 144204, <https://doi.org/10.1016/j.scitotenv.2020.144204>.
- [14] A.D. Igalavithana, S. Mandal, N.K. Niazi, M. Vithanage, S.J. Parikh, F.N. D. Mukome, M. Rizwan, P. Oleszczuk, M. Al-Wabel, N. Bolan, D.C.W. Tsang, K. H. Kim, Y.S. Ok, Advances and future directions of biochar characterization methods and applications, *Crit. Rev. Environ. Sci. Technol.* 47 (2017) 2275–2330, <https://doi.org/10.1080/10643389.2017.1421844>.
- [15] G. Song, F.Z. Qin, J.F. Yu, L. Tang, Y. Pang, C. Zhang, J.J. Wang, L.F. Deng, Tailoring biochar for persulfate-based environmental catalysis: Impact of biomass feedstocks, *J. Hazard. Mater.* 424 (2022), 127663, <https://doi.org/10.1016/j.jhazmat.2021.127663>.
- [16] J.M. Yuan, Y.H. Wen, D.D. Dionysiou, V.K. Sharma, X.M. Ma, Biochar as a novel carbon-negative electron source and mediator: electron exchange capacity (EEC) and environmentally persistent free radicals (EPFRs): a review, *Chem. Eng. J.* 429 (2022), 132313, <https://doi.org/10.1016/j.cej.2021.132313>.
- [17] Y. Wu, J. Guo, Y.J. Han, J.Y. Zhu, L.X. Zhou, Y.Q. Lan, Insights into the mechanism of persulfate activated by rice straw biochar for the degradation of aniline, *Chemosphere* 200 (2018) 373–379, <https://doi.org/10.1016/j.chemosphere.2018.02.110>.
- [18] C. Sun, T. Chen, Q.X. Huang, X.G. Duan, M.X. Zhan, L.J. Ji, X.D. Li, J.H. Yan, Selective production of singlet oxygen from zinc-etching hierarchically porous biochar for sulfamethoxazole degradation, *Environ. Pollut.* 290 (2021), 117991, <https://doi.org/10.1016/j.envpol.2021.117991>.
- [19] W.J. Liu, C.Y. Nie, W.L. Li, Z.M. Ao, S.B. Wang, T.C. An, Oily sludge derived carbons as peroxymonosulfate activators for removing aqueous organic pollutants: Performances and the key role of carbonyl groups in electron-transfer mechanism, *J. Hazard. Mater.* 414 (2021), 125552, <https://doi.org/10.1016/j.jhazmat.2021.125552>.
- [20] H. Meng, C.Y. Nie, W.L. Li, X.G. Duan, B. Lai, Z.M. Ao, S.B. Wang, T.C. An, Insight into the effect of lignocellulosic biomass source on the performance of biochar as persulfate activator for aqueous organic pollutants remediation: epicarp and mesocarp of citrus peels as examples, *J. Hazard. Mater.* 399 (2020), 123043, <https://doi.org/10.1016/j.jhazmat.2020.123043>.
- [21] K.M. Zhu, X.S. Wang, M.Z. Geng, D. Chen, H. Lin, H. Zhang, Catalytic oxidation of clofibric acid by peroxydisulfate activated with wood-based biochar: Effect of biochar pyrolysis temperature, performance and mechanism, *Chem. Eng. J.* 374 (2019) 1253–1263, <https://doi.org/10.1016/j.cej.2019.06.006>.
- [22] A.M. Clurman, O.M. Rodriguez-Narvaez, A. Jayarathne, G. De Silva, M. I. Ranasinghe, A. Goonetilleke, E.R. Bandala, Influence of surface hydrophobicity/hydrophilicity of biochar on the removal of emerging contaminants, *Chem. Eng. J.* 402 (2020), 126277, <https://doi.org/10.1016/j.cej.2020.126277>.
- [23] F. Xiao, A review of biochar functionalized by thermal air oxidation, *Environ. Funct. Mater.* 1 (2022) 187–195, <https://doi.org/10.1016/j.efmat.2022.03.001>.
- [24] D.G. Kim, S.O. Ko, Effects of thermal modification of a biochar on persulfate activation and mechanisms of catalytic degradation of a pharmaceutical, *Chem. Eng. J.* 399 (2020), 125377, <https://doi.org/10.1016/j.cej.2020.125377>.
- [25] Z.H. Wan, Z.B. Xu, Y.Q. Sun, M.J. He, D.Y. Hou, X.D. Cao, D.C.W. Tsang, Critical impact of nitrogen vacancies in nonradical carbocatalysis on nitrogen-doped graphitic biochar, *Environ. Sci. Technol.* 55 (2021) 7004–7014, <https://doi.org/10.1021/acs.est.0c08531>.
- [26] E.T. Yun, G.H. Moon, H. Lee, T.H. Jeon, C. Lee, W. Choi, J. Lee, Oxidation of organic pollutants by peroxymonosulfate activated with low-temperature-modified nanodiamonds: Understanding the reaction kinetics and mechanism, *Appl. Catal. B Environ.* 237 (2018) 432–441, <https://doi.org/10.1016/j.apcatb.2018.04.067>.
- [27] X. Chen, W.D. Oh, Z.T. Hu, Y.M. Sun, R.D. Webster, S.Z. Li, T.T. Lim, Enhancing sulfacetamide degradation by peroxymonosulfate activation with N-doped graphene produced through delicately-controlled nitrogen functionalization via tweaking thermal annealing processes, *Appl. Catal. B Environ.* 225 (2018) 243–257, <https://doi.org/10.1016/j.apcatb.2017.11.071>.
- [28] J. Miao, W. Geng, P.J.J. Alvarez, M.C. Long, 2D N-Doped porous carbon derived from polydopamine-coated graphitic carbon nitride for efficient nonradical activation of peroxymonosulfate, *Environ. Sci. Technol.* 54 (2020) 8473–8481, <https://doi.org/10.1021/acs.est.0c03207>.
- [29] J. Liang, X.Y. Xu, Q.J. Zhong, Z.B. Xu, L. Zhao, H. Qiu, X.D. Cao, Roles of the mineral constituents in sludge-derived biochar in persulfate activation for phenol degradation, *J. Hazard. Mater.* 398 (2020), 122861, <https://doi.org/10.1016/j.jhazmat.2020.122861>.
- [30] X.H. Wang, P. Zhang, C.P. Wang, H.Z. Jia, X.F. Shang, J.C. Tang, H.W. Sun, Metal-rich hyperaccumulator-derived biochar as an efficient persulfate activator: Role of intrinsic metals (Fe, Mn and Zn) in regulating characteristics, performance and

- reaction mechanisms, *J. Hazard. Mater.* 424 (2022), 127225, <https://doi.org/10.1016/j.jhazmat.2021.127225>.
- [31] A. Oya, S. Otani, Catalytic graphitization of carbons by various metals, *Carbon* 17 (1979) 131–137, [https://doi.org/10.1016/0008-6223\(79\)90020-4](https://doi.org/10.1016/0008-6223(79)90020-4).
- [32] S.M. Shaheen, Natasha, A. Mosa, A. El-Naggar, M.F. Hossain, H. Abdelrahman, N. K. Niazi, M. Shahid, T. Zhang, Y.F. Tsang, L. Trakal, S.S. Wang, J. Rinklebe, Manganese oxide-modified biochar: production, characterization and applications for the removal of pollutants from aqueous environments - a review, *Bioresour. Technol.* 346 (2022), 126581, <https://doi.org/10.1016/j.biortech.2021.126581>.
- [33] Y. Qiu, Q. Zhang, Z.H. Wang, B. Gao, Z.X. Fan, M. Li, H.R. Hao, X.N. Wei, M. Zhong, Degradation of anthraquinone dye reactive blue 19 using persulfate activated with Fe/Mn modified biochar: radical/non-radical mechanisms and fixed-bed reactor study, *Sci. Total Environ.* 758 (2021), 143584, <https://doi.org/10.1016/j.scitotenv.2020.143584>.
- [34] F.K. Yu, Y. Song, Y.P. Guo, J. Yang, Degradation of tetracycline by persulfate oxidation promoted by iron-modified biochar, *N. J. Chem.* 46 (2022) 22459–22468, <https://doi.org/10.1039/D2NJ03348H>.
- [35] F.S. Mustafa, K.H.H. Aziz, Heterogeneous catalytic activation of persulfate for the removal of rhodamine B and diclofenac pollutants from water using iron-impregnated biochar derived from the waste of black seed pomace, *Proc. Saf. Environ. Prot.* 170 (2023) 436–448, <https://doi.org/10.1016/j.psep.2022.12.030>.
- [36] C.J. Liang, C.F. Huang, N. Mohanty, R.M. Kurakalva, A rapid spectrophotometric determination of persulfate anion in ISCO, *Chemosphere* 73 (2008) 1540–1543, <https://doi.org/10.1016/j.chemosphere.2008.08.043>.
- [37] H.Y. Gao, C.H. Huang, L. Mao, B. Shao, Z.Y. Yan, M. Tang, B.Z. Zhu, First direct and unequivocal electron spin resonance spin-trapping evidence for pH-dependent production of hydroxyl radicals from sulfate radicals, *Environ. Sci. Technol.* 54 (2020) 14046–14056, <https://doi.org/10.1021/acs.est.0c04410>.
- [38] D. Ouyang, Y. Chen, J.C. Yan, L.B. Qian, L. Han, M.F. Chen, Activation mechanism of peroxymonosulfate by biochar for catalytic degradation of 1,4-dioxane: Important role of biochar defect structures, *Chem. Eng. J.* 370 (2019) 614–624, <https://doi.org/10.1016/j.cej.2019.03.235>.
- [39] L. Du, W.H. Xu, S.B. Liu, X. Li, D.L. Huang, X.F. Tan, Y.G. Liu, Activation of persulfate by graphitized biochar for sulfamethoxazole removal: The roles of graphitic carbon structure and carbonyl group, *J. Colloid Interf. Sci.* 577 (2020) 419–430, <https://doi.org/10.1016/j.jcis.2020.05.096>.
- [40] M.W. Smith, I. Dallmeyer, T.J. Johnson, C.S. Brauer, J.S. McEwen, J.F. Espinal, M. Garcia-Perez, Structural analysis of char by Raman spectroscopy: Improving band assignments through computational calculations from first principles, *Carbon* 100 (2016) 678–692, <https://doi.org/10.1016/j.carbon.2016.01.031>.
- [41] C.Q. Wang, R. Huang, R.R. Sun, J.P. Yang, M. Sillanpää, A review on persulfates activation by functional biochar for organic contaminants removal: Synthesis, characterizations, radical determination, and mechanism, *J. Environ. Chem. Eng.* 9 (2021), 106267, <https://doi.org/10.1016/j.jece.2021.106267>.
- [42] T.X. Yang, J. Meng, P. Jeyakumar, T. Cao, Z.Q. Liu, T.Y. He, X.N. Cao, W.F. Chen, H.L. Wang, Effect of pyrolysis temperature on the bioavailability of heavy metals in rice straw-derived biochar, *Environ. Sci. Pollut. Res.* 28 (2021) 2198–2208, <https://doi.org/10.1007/s11356-020-10193-5>.
- [43] R. Janu, V. Mrlik, D. Ribitsch, J. Hofman, P. Sedláček, L. Bielská, G. Soja, Biochar surface functional groups as affected by biomass feedstock, biochar composition and pyrolysis temperature, *Carbon Resour. Convers.* 4 (2021) 36–46, <https://doi.org/10.1016/j.crcon.2021.01.003>.
- [44] J. Wang, Z.W. Liao, J. Iftikhar, L.R. Shi, Z.Q. Chen, Z.L. Chen, One-step preparation and application of magnetic sulfur-derived biochar on acid orange 7 removal via both adsorption and persulfate based oxidation, *RSC Adv.* 7 (2017) 18696–18706, <https://doi.org/10.1039/C7RA01425B>.
- [45] A. Lange, H.D. Brauer, On the formation of dioxiranes and of singlet oxygen by the ketone-catalysed decomposition of Caro's acid, *J. Chem. Soc. Perk. Trans.* 2 (1996) 805–811, <https://doi.org/10.1039/P29960000805>.
- [46] R.D. Hunter, J. Ramirez-Rico, Z. Schnepf, Iron-catalyzed graphitization for the synthesis of nanostructured graphitic carbons, *J. Mater. Chem. A* 10 (2022) 4489–4516, <https://doi.org/10.1039/D1TA09654K>.
- [47] Y.F. Du, M. Dai, I. Naz, X.Y. Hao, X.X. Wei, R. Rong, C.S. Peng, I. Ali, Carbothermal reduction synthesis of zero-valent iron and its application as a persulfate activator for ciprofloxacin degradation, *Sep. Purif. Technol.* 275 (2021), 119201, <https://doi.org/10.1016/j.seppur.2021.119201>.
- [48] Q.G. Yan, C.X. Wan, J. Liu, J.S. Gao, F. Yu, J.L. Zhang, Z.Y. Cai, Iron nanoparticles in situ encapsulated in biochar-based carbon as an effective catalyst for the conversion of biomass-derived syngas to liquid hydrocarbons, *Green. Chem.* 15 (2013) 1631–1640, <https://doi.org/10.1039/C3GC37107G>.
- [49] S.J. Zhu, W. Wang, Y.P. Xu, Z.G. Zhu, Z.Q. Liu, F.Y. Cui, Iron sulfide-derived magnetic Fe⁰/Fe₃C catalyst for oxidation of ciprofloxacin via peroxymonosulfate activation, *Chem. Eng. J.* 365 (2019) 99–110, <https://doi.org/10.1016/j.cej.2019.02.011>.
- [50] E.T. Yun, S.W. Park, H.J. Shin, H. Lee, D.W. Kim, J. Lee, Peroxymonosulfate activation by carbon-encapsulated metal nanoparticles: Switching the primary reaction route and increasing chemical stability, *Appl. Catal. B Environ.* 279 (2020), <https://doi.org/10.1016/j.apcatb.2020.119360>.
- [51] L.K. Chen, Y.F. Huang, M.L. Zhou, K.W. Xing, W.Y. Lv, W.T. Wang, H.X. Chen, Y. Y. Yao, Nitrogen-doped porous carbon encapsulating iron nanoparticles for enhanced sulfathiazole removal via peroxymonosulfate activation, *Chemosphere* 250 (2020), 126300, <https://doi.org/10.1016/j.chemosphere.2020.126300>.
- [52] E. Thompson, A.E. Danks, L. Bourgeois, Z. Schnepf, Iron-catalyzed graphitization of biomass, *Green. Chem.* 17 (2015) 551–556, <https://doi.org/10.1039/C4GC01673D>.
- [53] M. Sevilla, A.B. Fuertes, Catalytic graphitization of templated mesoporous carbons, *Carbon* 44 (2006) 468–474, <https://doi.org/10.1016/j.carbon.2005.08.019>.
- [54] X. Jiao, Y.S. Qiu, L.Y. Zhang, X.D. Zhang, Comparison of the characteristic properties of reduced graphene oxides synthesized from natural graphites with different graphitization degrees, *RSC Adv.* 7 (2017) 52337–52344, <https://doi.org/10.1039/C7RA10809E>.
- [55] J. Campos-Delgado, H. Farhat, Y.A. Kim, A. Reina, J. Kong, M. Endo, H. Muramatsu, T. Hayashi, H. Terrones, M. Terrones, M.S. Dresselhaus, Resonant Raman study on bulk and isolated graphitic nanoribbons, *Small* 5 (2009) 2698–2702, <https://doi.org/10.1002/sml.200901059>.
- [56] B.J. Matos, K. Ranganathan, B.K. Mutuma, T. Leretholi, G. Jones, N.J. Coville, Time-dependent evolution of the nitrogen configurations in N-doped graphene films, *RSC Adv.* 6 (2016) 106914–106920, <https://doi.org/10.1039/C6RA24094A>.
- [57] Q. Chang, C.H. Zhang, C.W. Liu, Y.X. Wei, A.V. Cheruvathur, A.I. Dugulan, J. W. Niemantsverdriet, X.W. Liu, Y.R. He, M. Qing, L.R. Zheng, Y.F. Yun, Y. Yang, Y. W. Li, Relationship between iron carbide phases (ϵ -Fe₂C, Fe₃C, and χ -Fe₅C₂) and catalytic performances of Fe/SiO₂ Fischer-Tropsch catalysts, *ACS Catal.* 8 (2018) 3304–3316, <https://doi.org/10.1021/acscatal.7b04085>.
- [58] A.V. Mokhov, P.M. Kartashov, T.A. Gornostaeva, A.P. Rybchuk, O.A. Bogatikov, Electron microscopy in the study of lunar regolith, *Crystallogr. Rep.* 66 (2021) 648–655, <https://doi.org/10.1134/S1066377421040143>.
- [59] P. Chindaprasit, U. Rattanasak, Eco-production of silica from sugarcane bagasse ash for use as a photochromic pigment filler, *Sci. Rep.* 10 (2020) 9890, <https://doi.org/10.1038/s41598-020-66885-y>.
- [60] X.Z. Guo, L. Zhu, W.Y. Li, H. Yang, Preparation of SiC powders by carbothermal reduction with bamboo charcoal as renewable carbon source, *J. Adv. Ceram.* 2 (2013) 128–134, <https://doi.org/10.1007/s40145-013-0050-4>.
- [61] K.R. Zhu, H. Xu, C.L. Chen, X.M. Ren, A. Alsaedi, T. Hayat, Encapsulation of Fe⁰-dominated Fe₃O₄/Fe⁰/Fe₃C nanoparticles into carbonized polydopamine nanospheres for catalytic degradation of tetracycline via persulfate activation, *Chem. Eng. J.* 372 (2019) 304–311, <https://doi.org/10.1016/j.cej.2019.04.157>.
- [62] E.T. Yun, H.Y. Yoo, H. Bae, H.I. Kim, J. Lee, Exploring the role of persulfate in the activation process: Radical precursor versus electron acceptor, *Environ. Sci. Technol.* 51 (2017) 10090–10099, <https://doi.org/10.1021/acs.est.7b02519>.
- [63] T.H. Jeon, H. Kim, H.I. Kim, W. Choi, Highly durable photoelectrochemical H₂O₂ production via dual photoanode and cathode processes under solar simulating and external bias-free conditions, *Energ. Environ. Sci.* 13 (2020) 1730–1742, <https://doi.org/10.1039/C9EE03154E>.
- [64] E.S. Odinga, M.G. Waigi, F.O. Gudda, J. Wang, B. Yang, X.J. Hu, S.Y. Li, Y.Z. Gao, Occurrence, formation, environmental fate and risks of environmentally persistent free radicals in biochars, *Environ. Int.* 134 (2020), 105172, <https://doi.org/10.1016/j.envint.2019.105172>.
- [65] G.D. Fang, J. Gao, C. Liu, D.D. Dionysiou, Y. Wang, D.M. Zhou, Key role of persistent free radicals in hydrogen peroxide activation by biochar: Implications to organic contaminant degradation, *Environ. Sci. Technol.* 48 (2014) 1902–1910, <https://doi.org/10.1021/es4048126>.
- [66] W. Wu, S.S. Zhu, X.C. Huang, W. Wei, C. Jin, B.J. Ni, Determination of instant components of biomass on the generation of persistent free radicals (PFRs) as critical redox sites in pyrogenic chars for persulfate activation, *Environ. Sci. Technol.* 55 (2021) 7690–7701, <https://doi.org/10.1021/acs.est.1c01882>.
- [67] L.Z. Sun, J.R. Bolton, Determination of the quantum yield for the photochemical generation of hydroxyl radicals in TiO₂ suspensions, *J. Phys. Chem.* 100 (1996) 4127–4134, <https://doi.org/10.1021/jp9505800>.
- [68] C.T. Guan, J. Jiang, S.Y. Pang, Y. Zhou, Y. Gao, J. Li, Z. Wang, Formation and control of bromate in sulfate radical-based oxidation processes for the treatment of waters containing bromide: a critical review, *Wat. Res.* 176 (2020), 115725, <https://doi.org/10.1016/j.watres.2020.115725>.
- [69] G.W. Klein, K. Bhatia, V. Madhavan, R.H. Schuler, Reaction of hydroxyl radicals with benzoic acid. Isomer distribution in the radical intermediates, *J. Phys. Chem.* 79 (1975) 1767–1774, <https://doi.org/10.1021/j100584a005>.
- [70] W.R. Haag, J. Hoigne, Singlet oxygen in surface waters. 3. Photochemical formation and steady-state concentrations in various types of waters, *Environ. Sci. Technol.* 20 (1986) 341–348, <https://doi.org/10.1021/es00146a005>.
- [71] J.C. Yan, L. Han, W.G. Gao, S. Xue, M.F. Chen, Biochar supported nanoscale zerovalent iron composite used as persulfate activator for removing trichloroethylene, *Bioresour. Technol.* 175 (2015) 269–274, <https://doi.org/10.1016/j.biortech.2014.10.103>.
- [72] Y. Li, Z.Q. Yang, H.G. Zhang, X.W. Tong, J.N. Feng, Fabrication of sewage sludge-derived magnetic nanocomposites as heterogeneous catalyst for persulfate activation of Orange G degradation, *Colloids Surf. A* 529 (2017) 856–863, <https://doi.org/10.1016/j.colsurfa.2017.06.043>.